



# Modal content of typhoon-induced near-inertial waves around the East China Sea

Anzhou Cao<sup>a,b</sup>, Shuya Wang<sup>b</sup>, Akihiko Morimoto<sup>b,\*</sup>, Tetsutaro Takikawa<sup>c</sup>, Xinyu Guo<sup>b</sup>

<sup>a</sup> Ocean College, Zhejiang University, Zhoushan, China

<sup>b</sup> Center for Marine Environmental Studies, Ehime University, Matsuyama, Japan

<sup>c</sup> Graduate School of Fisheries and Environmental Sciences, Nagasaki University, Nagasaki, Japan

## ARTICLE INFO

### Keywords:

Near-inertial waves  
Modal content  
East China Sea  
Modal wind forcing  
Two-layer-structure stratification

## ABSTRACT

Recent studies show that typhoon-induced near-inertial waves (NIWs) exhibit different modal content in the shallow and deep regions, whereas the underlying mechanism has not been fully understood. Based on a three-dimensional numerical model, we simulate the NIWs induced by two typhoons (Songda and Meari in 2011) in the East China Sea and its adjacent deep waters in the northwest Pacific Ocean. Although the near-inertial kinetic energy induced by the two typhoons has different intensity and spatial distribution, the modal content of NIWs induced by them shares a common characteristic: In the shallow regions (water depth smaller than 200 m), the NIWs are mainly dominated by mode-1; whereas in the deep regions (water depth larger than 200 m), the NIWs are dominated by higher modes (mode-2 to mode-5). Different mechanisms are found to account for the different modal content in shallow and deep regions. The dominance of higher-mode wind forcing is the cause for the dominance of higher-mode NIWs in the deep regions. The two-layer-structure stratification is the cause for the dominance of mode-1 NIWs in the shallow regions.

## 1. Introduction

Near-inertial waves (NIWs) are internal waves with frequency close to the local Coriolis frequency, which are mainly caused by winds and are ubiquitous in the global ocean. As a predominant peak in the internal wave spectrum, NIWs make significant contributions to the turbulent mixing in the ocean (Alford et al., 2016; Mackinnon et al., 2017; Whalen et al., 2020). The global wind power input to near-inertial motions is 0.3–1.5 TW (Alford, 2003, 2020; Jiang et al., 2005; Furuichi et al., 2008; Liu et al., 2019), which is comparable to that converted from astronomical tides to internal tides (Munk and Wunsch, 1998; Simmons et al., 2004; Niwa and Hibiya, 2011).

Typhoons are particularly efficient generators of NIWs owing to their strong wind stresses and compact size (Alford et al., 2016). Typhoon-induced NIWs are generally characterized by upgoing phase and hence downgoing energy (e.g. Alford et al., 2012; Guan et al., 2014; Le Boyer et al., 2020). Observations have indicated that the vertical scales of typhoon-induced NIWs are approximately ranging from 100 to 600 m (Alford et al., 2012; Cao et al., 2018; Yu et al., 2022). Typhoon-induced NIWs can persist for several to more than 10 days after the passage of the typhoon (e.g. Chen et al., 2013; Guan et al., 2014; Cao

et al., 2018; Qiao et al., 2022). Furthermore, other ocean dynamical processes, such as the large-scale circulations and mesoscale eddies, can modulate the propagation and dissipation of NIWs (Chen et al., 2013; Jeon et al., 2019a; Kawaguchi et al., 2020; Sanford et al., 2021; He et al., 2022).

Typhoon-induced NIWs are certainly related to the typhoon characteristics, such as the maximum sustained wind speed, radius of the maximum sustained wind speed, typhoon translation speed and typhoon track (e.g. Chen et al., 2015). The ocean stratification can also influence their characteristics (Jeon et al., 2019b). Recent studies show that the typhoon-induced NIWs show apparent differences in shallow and deep regions. One significant difference is the dominant mode of NIWs. The NIWs in shallow regions are usually dominated by mode-1 (Yang et al., 2015, 2021; Zhang et al., 2018; de Freitas et al., 2019; Schlosser et al., 2019), whereas higher modes account for more of the total near-inertial kinetic energy (NIKE) than mode-1 in deep regions (He et al., 2022; Raja et al., 2022). However, the underlying mechanism has not been fully understood.

In this study, we choose the East China Sea (ECS) and its adjacent deep waters in the northwest Pacific Ocean to study the modal content of typhoon-induced NIWs based on the numerical simulation. Two

\* Corresponding author.

E-mail address: [morimoto.akhiko.cl@ehime-u.ac.jp](mailto:morimoto.akhiko.cl@ehime-u.ac.jp) (A. Morimoto).

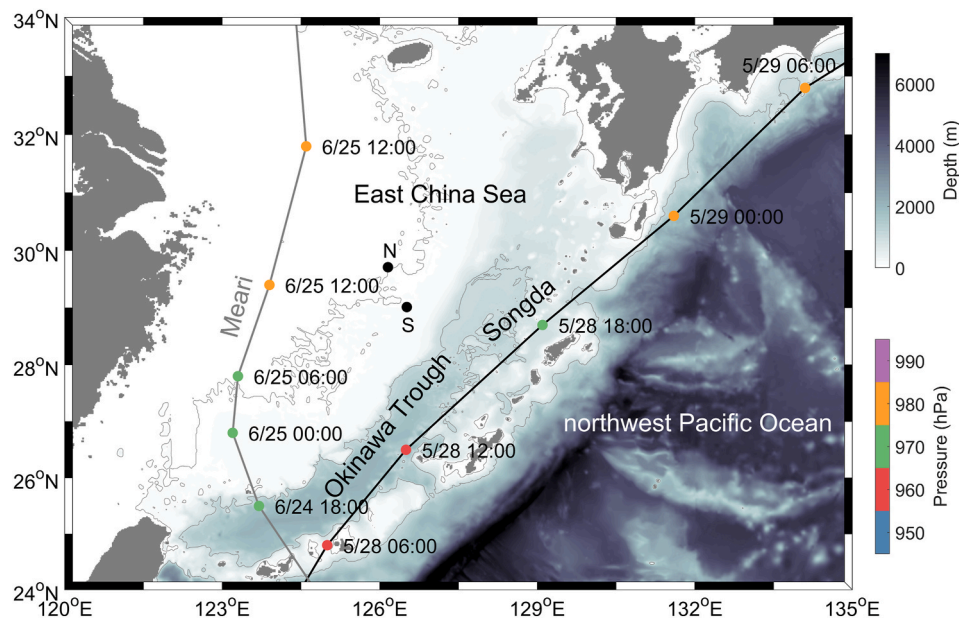


**Fig. 1.** Bathymetry of the domain. The two black dots indicate the locations of two moorings. The black and gray curves represent the tracks of typhoons Songda and Meari in 2011, respectively. The colored dots indicate the typhoon central pressure. Time is labeled every 6 h.

moorings deployed on the continental shelf of ECS captured the passage of typhoons Songda and Meari in 2011, which provide the data for model validation. The paper is organized as follows. The two typhoons, moored observations, model configurations and data analysis methods are introduced in section 2. The main results are shown in section 3, including the validation of simulated results, NIKE, and modal content and wave characteristics of NIWs induced by the typhoons. In section 4, the mechanisms for different modal content of NIWs in shallow and deep regions are discussed. Finally, a summary completes the paper in section 5.

## 2. Data and methodology

### 2.1. Typhoons Songda and Meari

Songda and Meari were the 2nd and 5th typhoons in the western Pacific Ocean in 2011. According to the best track data from the China Meteorological Administration tropical cyclone database ([tcdata.typhoon.org.cn](http://tcdata.typhoon.org.cn), Ying et al., 2014), Songda entered the domain on May 28 with the central pressure of 960 hPa (Fig. 1). Thereafter, it moved northeastward and left the domain on May 29. During this period, the maximum sustained wind speed of Songda decreased from 40 to 25 m/s and the central pressure increased from 960 to 980 hPa. Compared with Songda, Meari was a little weaker, with the maximum sustained wind speed of approximately 30 m/s. It entered the domain on June 24 and left the domain on June 25. Unlike Songda which moved northeastward, Meari's track was nearly northward.

### 2.2. Moored observations

Two moorings were deployed on the continental shelf of ECS from May 28 to July 2, 2011, which captured the passage of the two typhoons. The two moorings were located at (126.5155°E, 29.0136°N) and (126.1568°E, 29.7089°N), where the water depth was approximately 113 and 87 m, respectively (Fig. 1). At the north (south) mooring, a WH-Sentinel 600 (300) kHz upward looking acoustic Doppler current profiler (ADCP, Teledyne RD Instruments) was equipped at the seafloor to measure velocities in the water column. The bin size of each ADCP was set to 4 m and the sampling time interval was 600 s. The standard deviation of measured velocities for error was smaller than 0.5 cm/s. The

ADCPs also measured the bottom pressure at the two moorings, from which the surface elevation can be obtained.

We used percent good which is the ratio of good pings per total pings for each ensemble average for data quality control. Velocities more than 90% of percent good were used for analysis. Magnetic north was converted to true north using geomagnetic data of Geospatial Information Authority of Japan.

Due to the poor data quality near the surface, the velocity observations in the upper layer were discarded. Thereafter, the moored velocity observations were linearly interpolated at uniform 4-m interval levels. Linear interpolation was used to fill in the gaps in the temporal domain, if the raw observations covered more than 95% of the total observation period at the corresponding depth (Cao et al., 2017). After this processing, the effective vertical range of velocities at the north (south) mooring was 28–80 (32–104) m. In this study, the observed velocities and surface elevations were used to validate the numerical simulation results.

### 2.3. Model configuration

The regional ocean modeling system (ROMS) under the framework of coastal and regional ocean community model (CROCO, [www.croco-ocean.org](http://www.croco-ocean.org)) was used to simulate the NIWs induced by typhoons Songda and Meari. The simulated domain was 116–134°E, 23–41°N with a uniform horizontal resolution of 1/10°. There were 30 uneven sigma layers in the vertical direction, with a finer resolution near the surface. The bathymetry used in the model was obtained from the ETOPO1 data (Amante and Eakins, 2009) and smoothed to minimize the horizontal pressure gradient error. To avoid artificial reflection of NIWs at the open boundaries, a 1° sponge layer was used to absorb the baroclinic energy.

The numerical simulation started on May 1, 2011 and ended on July 31, 2011. The initial conditions including the water temperature, salinity, sea surface height and background currents on 1 May 2011 were obtained from the hybrid coordinate ocean model (HYCOM) reanalysis results downloaded from the Asia-Pacific Data-Research Center ([apdrc.soest.hawaii.edu/data/data.php](http://apdrc.soest.hawaii.edu/data/data.php)). At the open boundaries, the surface elevations and barotropic currents of the eight principle tidal constituents ( $K_1$ ,  $O_1$ ,  $P_1$ ,  $Q_1$ ,  $M_2$ ,  $S_2$ ,  $N_2$  and  $K_2$ ) extracted from the Oregon State University global models of ocean tides (TPX07; Egbert

and Erofeeva, 2002) were introduced into the model via the Flather radiative conditions. The daily temperature, salinity and background currents from the HYCOM reanalysis results were introduced into the model via a nudging scheme. The hourly Climate Forecast System Reanalysis (CFSR) winds downloaded from the Asia-Pacific Data-Research Center were used as the surface forcing. Through a comparison with the maximum sustained wind speed of the two typhoons from the best track data, we found that the CFSR winds were a little smaller. Hence, the CFSR winds were amplified by a factor of 1.2 when used in the CROCO. The wind stress drag coefficient developed by Oey et al. (2006) was used to calculate the wind stress. The Large-/McWilliams/Doney K-profile parameterization mixing scheme (Large et al., 1994) was used for vertical turbulent mixing of momentum and tracers. The lateral viscosity and bottom friction coefficient was set to  $10 \text{ m}^2/\text{s}$  and 0.0025, respectively. The simulated results were output every hour. This experiment was named as “FULL run”.

Because the local Coriolis frequency near  $30^\circ\text{N}$  is close to those of diurnal tidal constituents, we cannot accurately extract typhoon-induced NIWs from FULL run (The same problem exists for the moored observations). Hence, another experiment named as “NO-TIDE run” was performed. The settings of NO-TIDE run were the same as those of FULL run except that there was no tidal forcing. In this study, the results of FULL run were used to compare with the moored observations to validate the numerical simulation, and the results of NO-TIDE run were used to study the NIWs induced by the two typhoons.

#### 2.4. Data analysis methods

The 4th order Butterworth filtering with cutoff frequency of  $[0.80, 1.20]f$  ( $f$  is the local Coriolis frequency) was used to extract the near-inertial velocities from the results of NO-TIDE run. The filtering was also operated twice with once forward and once backward. Thereafter, modal decomposition was carried out:

$$\begin{cases} u_f(z, t) = \sum_{m=0}^M u_{fm}(z, t) = \sum_{m=0}^M \hat{u}_{fm}(t) \Pi_m(z) \\ v_f(z, t) = \sum_{m=0}^M v_{fm}(z, t) = \sum_{m=0}^M \hat{v}_{fm}(t) \Pi_m(z) \end{cases}, \quad (1)$$

where  $z$  is the depth,  $t$  is the time,  $u_f$  and  $v_f$  are the filtered zonal and meridional near-inertial velocities,  $u_{fm}$  and  $v_{fm}$  are the zonal and meridional modal near-inertial velocities with respect to mode  $m$  ( $m = 0$  for the barotropic mode and  $m > 0$  for baroclinic modes),  $\hat{u}_{fm}$  and  $\hat{v}_{fm}$  are the corresponding modal amplitudes of  $u_{fm}$  and  $v_{fm}$ , and  $\Pi_m$  is the  $m$ -th normal mode:

$$\Pi_m(z) = \rho_0 c_m^2 \frac{d\Phi_m(z)}{dz}, \quad (2)$$

in which  $\rho_0$  is the reference density,  $\Phi_m(z)$  is the eigenfunction of eigenvalue problem for eigenspeed  $c_m$ :

$$\frac{d^2 \Phi_m}{dz^2} + \frac{N^2}{c_m^2} \Phi_m = 0, \quad (3)$$

subject to boundary conditions  $\Phi_m(0) = \Phi_m(-H) = 0$ , in which  $N$  is the local buoyancy frequency and  $H$  is the water depth. Based on the simulated temperature and salinity, the potential density and buoyancy frequency were easily obtained, and the normal mode  $\Pi_m$  was then calculated according to Equations (2) and (3). Using the least squares method and filtered near-inertial velocities,  $\hat{u}_{fm}$  and  $\hat{v}_{fm}$  were obtained according to Equation (1) (e.g. Zhao et al., 2010; Cao et al., 2015; He et al., 2022). Multiplying  $\hat{u}_{fm}$  ( $\hat{v}_{fm}$ ) by  $\Pi_m$ , the modal near-inertial velocities were finally obtained. Considering that the water depth varies significantly in the domain (Fig. 1), we first divided the domain into shallow ( $H \leq 200 \text{ m}$ ) and deep ( $H > 200 \text{ m}$ ) regions and then adopted the following strategy to conduct modal decomposition: For  $H < 50 \text{ m}$ ,

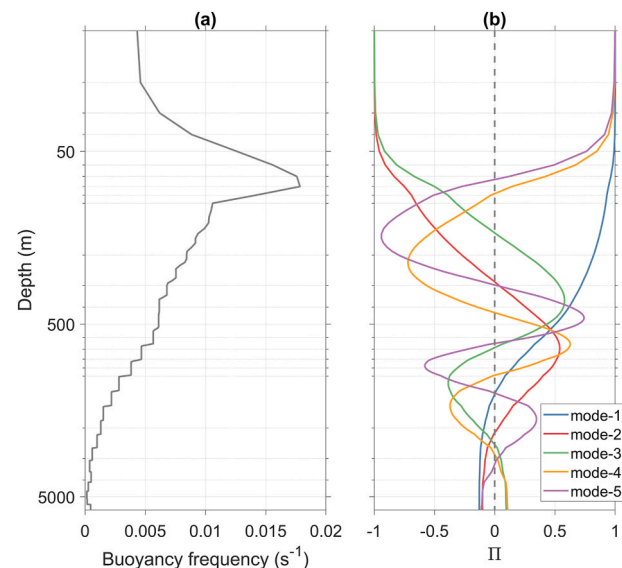


Fig. 2. (a) Buoyancy frequency and (b) the first five baroclinic modes at  $128^\circ\text{E}$ ,  $24.8^\circ\text{N}$ . Note that the y-axes are in the log form.

modal decomposition was not conducted; For  $50 \leq H \leq 200 \text{ m}$  ( $H > 200 \text{ m}$ ), the simulated temperature, salinity and near-inertial velocities were first interpolated at 20 uniform layers between the surface and seafloor (uniform 10-m layers), and then modal decomposition was conducted. Following Raja et al. (2022), the first five baroclinic modes were considered in this study. Fig. 2 shows the buoyancy frequency and normal modes ( $\Pi_m$ ) at  $128^\circ\text{E}$ ,  $24.8^\circ\text{N}$  as an example. Note that  $\Pi_m$  has been normalized in this study.

Based on the filtered near-inertial velocities (modal decomposition results), the NIKE (modal NIKE) can be calculated as:

$$\text{NIKE} = \frac{1}{2} \rho_0 (u_f^2 + v_f^2) \quad \text{and} \quad \text{NIKE}_m = \frac{1}{2} \rho_0 (u_{fm}^2 + v_{fm}^2). \quad (4)$$

The wind power input (WPI) to near-inertial motions is defined as:

$$\text{WPI} = \boldsymbol{\tau} \bullet \mathbf{u}_f(z=0), \quad (5)$$

where  $\boldsymbol{\tau}$  is the near-inertial wind stress vector and  $\mathbf{u}_f$  is the near-inertial velocity vector. Following Furuichi et al. (2008) and Raja et al. (2022), the modal WPI was calculated:

$$\text{WPI}_m = \boldsymbol{\tau} \bullet \mathbf{u}_{fm}(z=0). \quad (6)$$

Frequency and wavenumber are important wave characteristics of NIWs. Based on the Wentzel-Kramers-Brillouin (WKB) scaling and plane-wave fitting, the frequency and vertical wavenumber in the WKB stretched depth coordinate can be estimated (Alford et al., 2012; Cao et al., 2018). The WKB stretched depth is calculated as:

$$z_{\text{WKB}} = \int_0^z N(z') / \bar{N} dz', \quad (7)$$

where  $N(z)$  is the local buoyancy frequency and  $\bar{N}$  is its mean value. In the WKB stretched depth coordinate, the zonal or meridional near-inertial velocities  $[\Psi(z_{\text{WKB}}, t)]$  can be fitted with the plane-wave equation based on the least squares method:

$$\Psi(z_{\text{WKB}}, t) = \text{Re}\{\Psi_0 \exp[i(\omega t - m_0 z_{\text{WKB}} - \varphi)]\}, \quad (8)$$

where  $\Psi_0$  is the amplitude,  $\omega$  is the frequency,  $m_0$  is the vertical wavenumber, and  $\varphi$  is the phase. Note that only the  $\omega$ ,  $m_0$  and  $\varphi$  were fitted in this study.

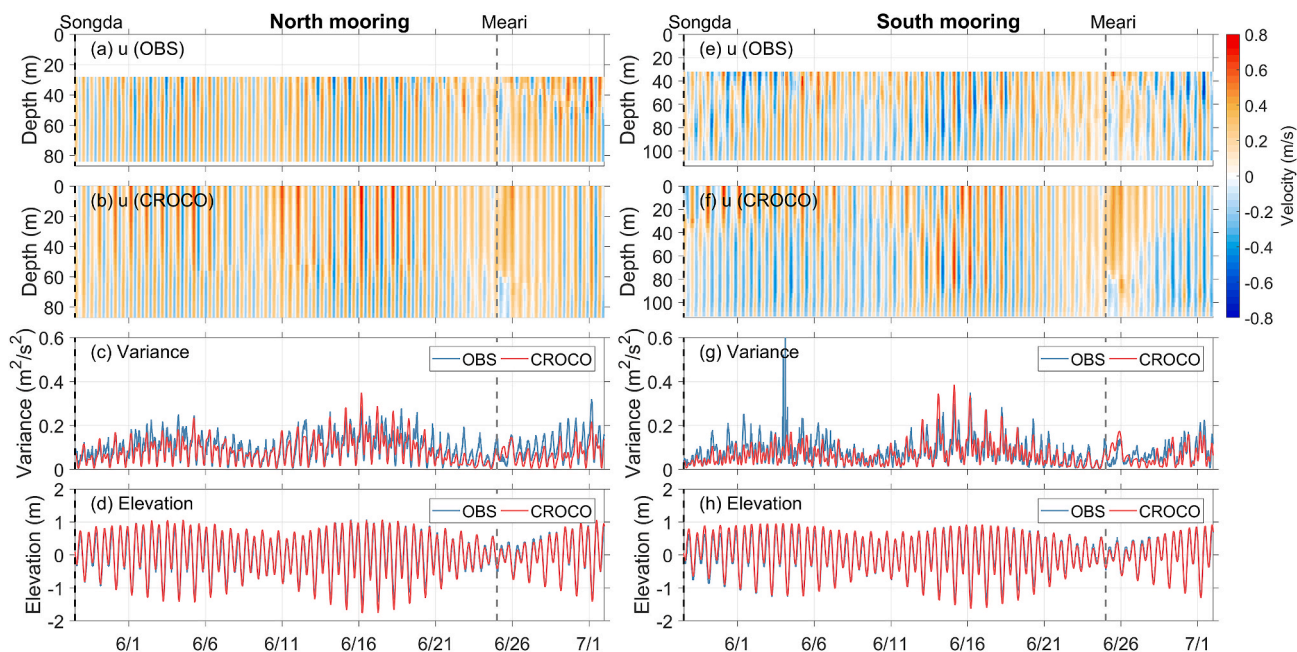


**Fig. 3.** Comparison between raw observations and simulated results of FULL run at the two moorings: (a, b, e, f) zonal velocities, (c, g) current variance averaged in the measuring range and (d, h) surface elevations at the (a–d) north and (e–h) south moorings. The vertical dashed lines indicate the time that the two typhoons passed by.

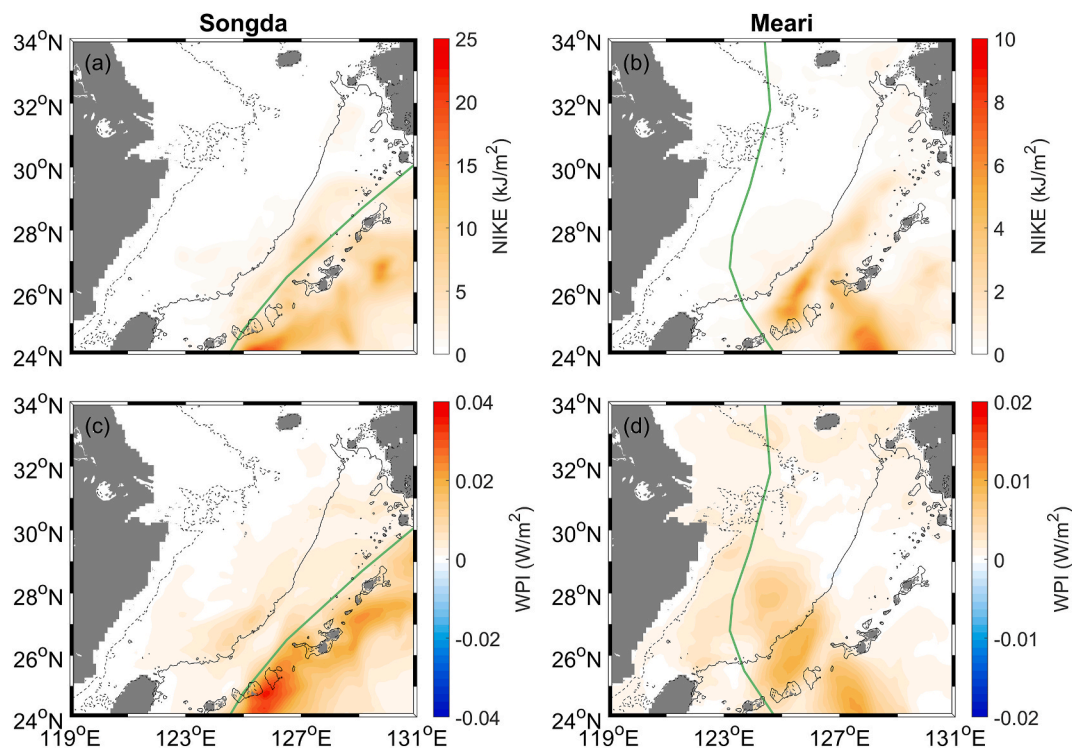


**Fig. 4.** Time-averaged (a, b) depth-integrated NIKE and (c, d) WPI for (a, c) Songda and (b, d) Meari. In each panel, the green curve denotes the typhoon track, and the black dashed and solid curves denote the 50 and 200 m isobaths, respectively.

### 3. Results

#### 3.1. Validation of simulated results

Fig. 3 compares the raw observations and simulated results of FULL run at the two moorings. On the whole, the observed velocities, current variance ( $\text{Var} = u^2 + v^2$ ) and surface elevations are generally reproduced

by the CROCO: The velocities, current variance and surface elevation show apparent spring-neap tidal cycles, suggesting that the motions at the two moorings are dominated by tides. After the passage of the two typhoons, the velocities in the upper layer are enhanced (Fig. 3b and f), indicating that the ocean dynamical response to the typhoons is successfully simulated by the CROCO. Given that the FULL run generally reproduces the motions at the two moorings, it is reasonable to use to

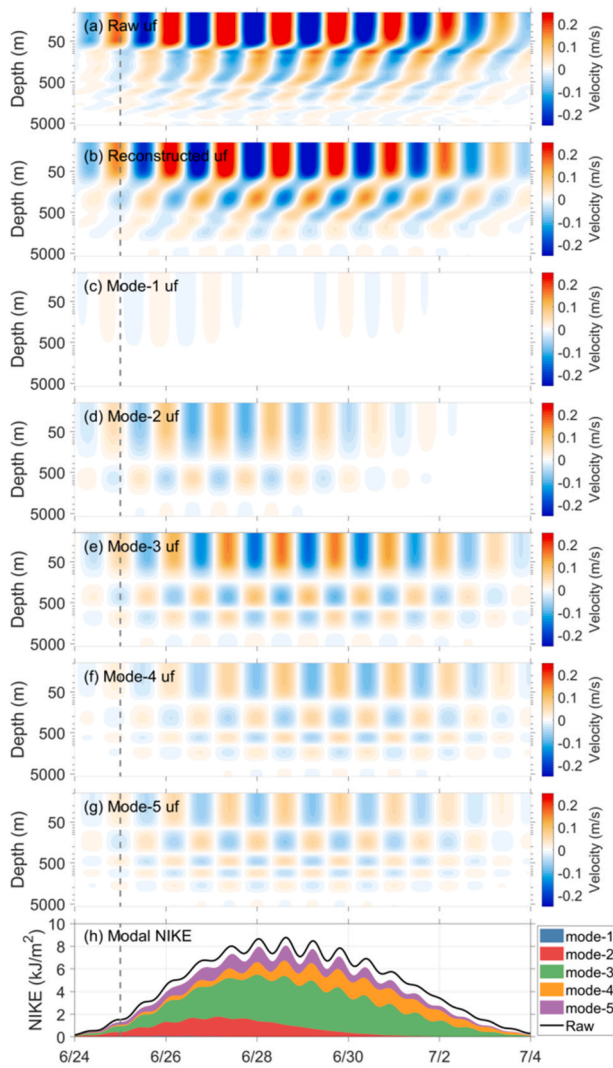


**Fig. 5.** (a) Raw zonal near-inertial velocities at 128°E, 24.8°N and (b) the reconstructed result by superposing (c–g) mode-1 to mode-5 zonal near-inertial velocities. (h) Depth-integrated NIKE and modal NIKE at this point. In each panel, the gray vertical dashed line indicates the time Meari passed by. Note that the y-axes of subfigures (a–g) are in the log form.

simulated results of NO-TIDE run to analyze the characteristics of NIWs induced by typhoons Songda and Meari.

### 3.2. Typhoon-induced NIKE

Fig. 4a and b show the time-averaged depth-integrated NIKE induced by Songda and Meari, respectively. The time range for averaging is from 00:00 on May 28 to 00:00 on June 9 (from 00:00 on June 25 to 00:00 on July 3) for Songda (Meari). It is clearly shown that large NIKE mainly appears to the right side of both typhoon tracks, which is consistent with the rightward biased feature of ocean response to typhoons in the Northern Hemisphere (Price et al., 1994). Because Songda is stronger than Meari, Songda-induced NIKE is also larger than that induced by Meari. The NIKE induced by the two typhoons also shares a common feature, i.e. the NIKE in the deep regions of the domain is apparently larger than that in the shallow regions. To be specific, the NIKE in the Okinawa Trough and northwest Pacific Ocean is much larger than that on the continental shelf of ECS. Fig. 4c and d illustrate the time-averaged WPI for Songda and Meari. It is easy to find that the WPI nearly shares the same pattern as the NIKE for both typhoons, suggesting that the NIKE is mainly generated locally.

### 3.3. Modal content of typhoon-induced NIWs

Fig. 5 shows the modal decomposition results of zonal near-inertial velocities as well as the modal NIKE induced by typhoon Meari at 128°E, 24.8°N as an example. It is clearly shown that the mode-3 dominates Meari-induced NIWs here. The mode-2, mode-4 and mode-5 near-inertial velocities are comparable but weaker than the mode-3. The mode-1 near-inertial velocities are much weaker than other modes. The proportions of the first five baroclinic modes in the total NIKE are 0.4%, 12.8%, 44.5%, 16.0% and 13.7%, respectively, and the sum of them exceeds 87%. As a result, the reconstructed near-inertial velocities (Fig. 5b), which are the superposition of mode-1 to mode-5, are nearly the same as the raw near-inertial velocities (Fig. 5a). This result validates the modal decomposition method. The slight deviation between the reconstructed and raw near-inertial velocities is related to the modes higher than mode-5, of which the total contribution to the total NIKE is smaller than 13%.

The time-averaged depth-integrated modal NIKE as well as the dominant mode of the first five baroclinic modes for Meari-induced NIWs are displayed in Fig. 6. It is easy to find that the distribution of mode-1 NIKE is different from those of the higher modes (mode-2 to mode-5). As shown in Fig. 6a, the mode-1 NIKE mainly appears in the shallow regions on the continental shelf of ECS and around the Ryukyu Islands, and that in the deep regions in the Okinawa Trough and northwest Pacific Ocean is too small to be detected. In contrast, higher-mode NIKE is mainly concentrated in the deep regions, and that in the shallow regions is nearly invisible (Fig. 6b–e). As a result, Meari-induced NIWs are mainly dominated by mode-1 in the shallow regions but higher modes in the deep regions. To be specific, mode-2 and mode-3 are dominant in the Okinawa Trough, and mode-3 to mode-5 are dominant in the northwest Pacific Ocean.

The modal NIKE and dominant mode for Songda-induced NIWs are shown in Fig. 7. Although the intensity and distribution of modal NIKE induced by Songda (Fig. 7a–e) vary from those induced by Meari (Fig. 6a–e), the distributions of dominant mode of NIWs induced by the two typhoons are similar (Fig. 6f and 7f). Combining these results, we can preliminarily conclude that the modal content of typhoon-induced NIWs are related to the local water depth. The underlying mechanisms will be discussed in Section 4.

### 3.4. Wave characteristics of typhoon-induced NIWs

Based on the WKB scaling and plane-wave fitting, we can obtain more wave characteristics of typhoon-induced NIWs. Fig. 8 shows the WKB scaling and plane-wave fitting results of Meari-induced NIWs at 128°E, 24.8°N as an example. According to Equation (7), if the stratification is larger (smaller) than the averaged stratification (Fig. 8a), the corresponding depth range would be extended (compressed) in the WKB stretched depth coordinate (Fig. 8b). Hence, transforming the near-inertial velocities from the depth coordinate (Fig. 8c) to the WKB stretched depth coordinate (Fig. 8d) reduces the influence of varying stratification in the vertical direction. As shown in Fig. 8e, the fitted NIWs generally show the same phase pattern as the observed NIWs in the WKB stretched depth coordinate (Fig. 8d), demonstrating the accuracy of plane-wave fitting. The fitted frequency ( $\omega$ ) and vertical wavenumber ( $m_0$ ) in the WKB stretched depth coordinate of Meari-induced NIWs here are  $6.17 \times 10^{-5} \text{ s}^{-1}$  (1.01 times the local Coriolis frequency  $f$ ) and  $1.40 \times 10^{-3} \text{ m}^{-1}$ . Hence, the vertical wavelength of Meari-induced NIWs is 4488 m in the WKB stretched depth coordinate. This value is generally consistent with the vertical wavelength of mode-3 (Table 1), the dominant mode here (Fig. 5). According to the dispersion relation of NIWs,

$$k_h^2 = \frac{m_0^2(\omega^2 - f^2)}{N^2}, \quad (9)$$

the horizontal wavenumber ( $k_h$ ) of Meari-induced NIWs here is  $7.47 \times 10^{-6} \text{ m}^{-1}$ , corresponding to the horizontal wavelength of 841 km. The

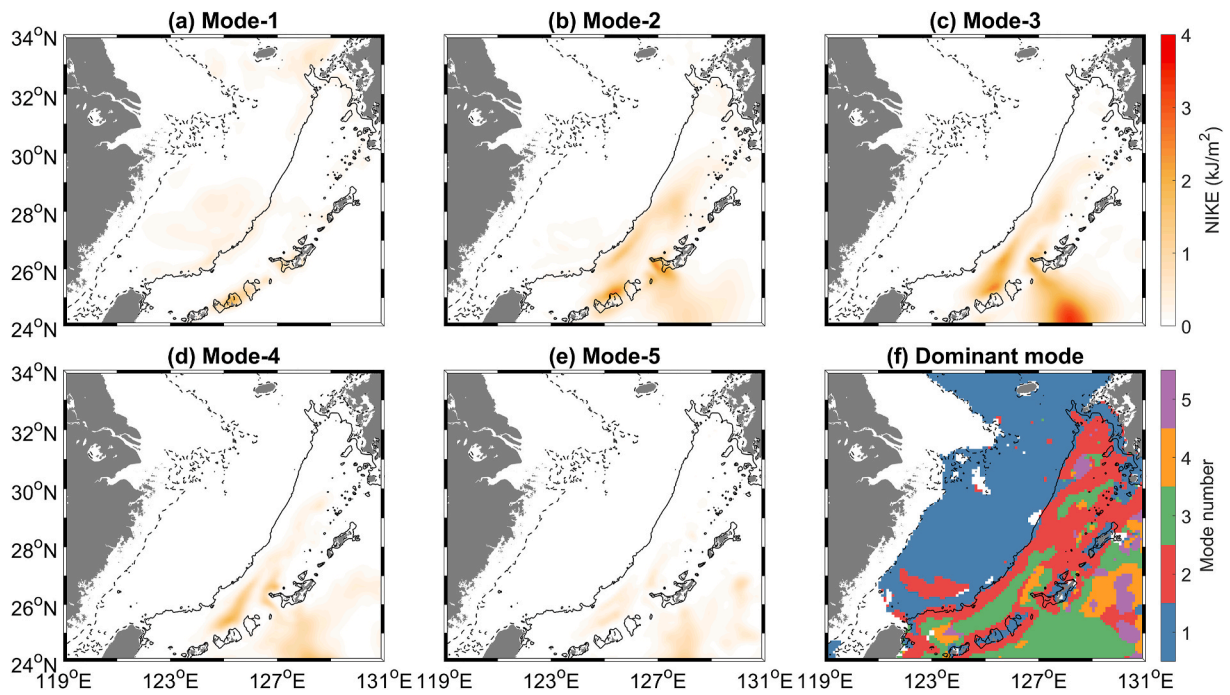


Fig. 6. Time-averaged depth-integrated modal NIKE of (a–e) mode-1 to mode-5 for Meari. (f) Dominant mode among the first five baroclinic modes of Meari-induced NIWs. The black dashed and solid curves denote the 50 and 200 m isobaths.

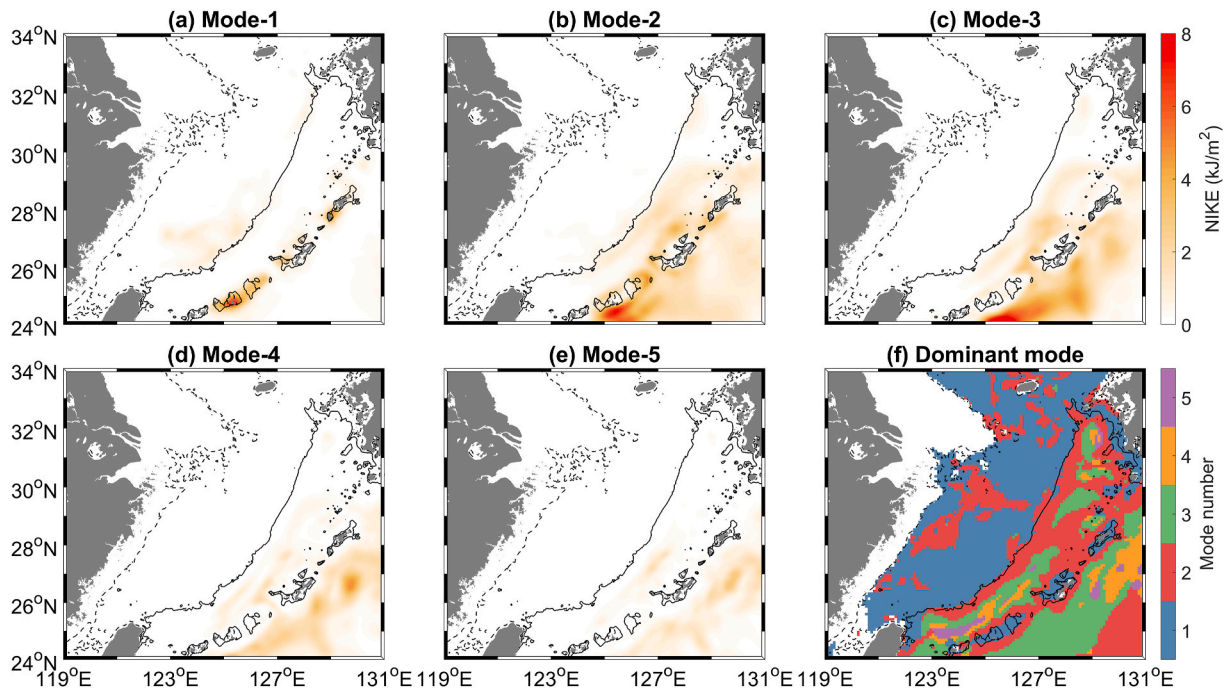


Fig. 7. Time-averaged depth-integrated modal NIKE of (a–e) mode-1 to mode-5 for Songda. (f) Dominant mode among the first five baroclinic modes of Songda-induced NIWs. The black dashed and solid curves denote the 50 and 200 m isobaths.

estimated frequency and horizontal wavenumber of NIWs generally satisfy the following equation (Kundu, 1993):

$$\omega = U_T k_h, \tag{10}$$

where  $U_T$  is the typhoon translation speed. The estimated  $U_T$  according to the frequency and horizontal wavenumber of NIWs is 8.25 m/s, and that calculated from the best track data is 5.2–12.1 m/s during 12:00 on June 24 to 18:00 on June 25. Moreover, according to Alford et al.

(2012),

$$c_{gz} = \frac{\omega^2 - f^2}{m_0 \omega}, \tag{11}$$

the estimated vertical group speed ( $c_{gz}$ ) of Meari-induced NIWs here is  $9.53 \times 10^{-4}$  m/s (approximately 82 m/day). Note that the aforementioned wave characteristics vary with locations, as the water depth, buoyancy frequency and dominant mode of NIWs are different. In

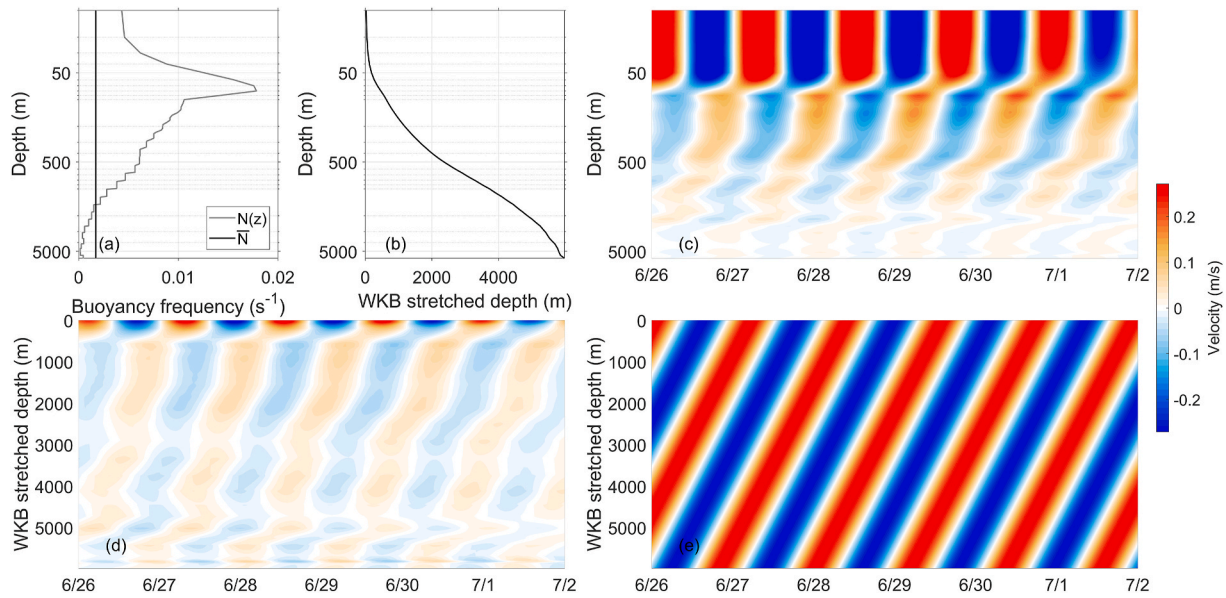


**Fig. 8.** (a) Stratification at 128°E, 24.8°N. (b) The WKB stretched depth according to the stratification. Zonal near-inertial velocities at 128°E, 24.8°N in the (c) depth coordinate and (d) WKB stretched depth coordinate. (e) Results of plane-wave fitting. Note that the y-axes of subfigures (a–c) are in the log form.

**Table 1**

Theoretical vertical wavelengths (unit: m, in the WKB stretched depth coordinate) of mode-1 to mode-5 at 128°E, 24.8°N.

Mode	Mode-1	Mode-2	Mode-3	Mode-4	Mode-5
Wavelength	12000	6000	4000	3000	2400

In addition, because the NIWs are dominated by mode-1 in the shallow regions, which exhibit mode-1 rather than beam-like structure, the WKB scaling and plane-wave fitting cannot be used in these regions.

#### 4. Discussion

The simulated results of NIWs induced by typhoon Songda and Meari show that the typhoon-induced NIWs are mainly dominated by mode-1 in the shallow regions of the domain but higher modes (mode-2 to mode-5) in the deep regions. Given that WPI can account for the typhoon-induced NIKE (section 3.2), attention is first paid to the modal WPI. Figs. 9 and 10 illustrate the modal WPI for typhoons Meari and Songda, respectively. It is clearly shown that the modal WPI almost shares the same pattern as the modal NIKE for all the first five baroclinic modes and for both typhoons (Figs. 6 and 7): Mode-1 WPI mainly appears in the shallow regions (on the continental shelf of ECS and around the Ryukyu Islands) and higher-mode WPI mainly appears in the deep regions (in the

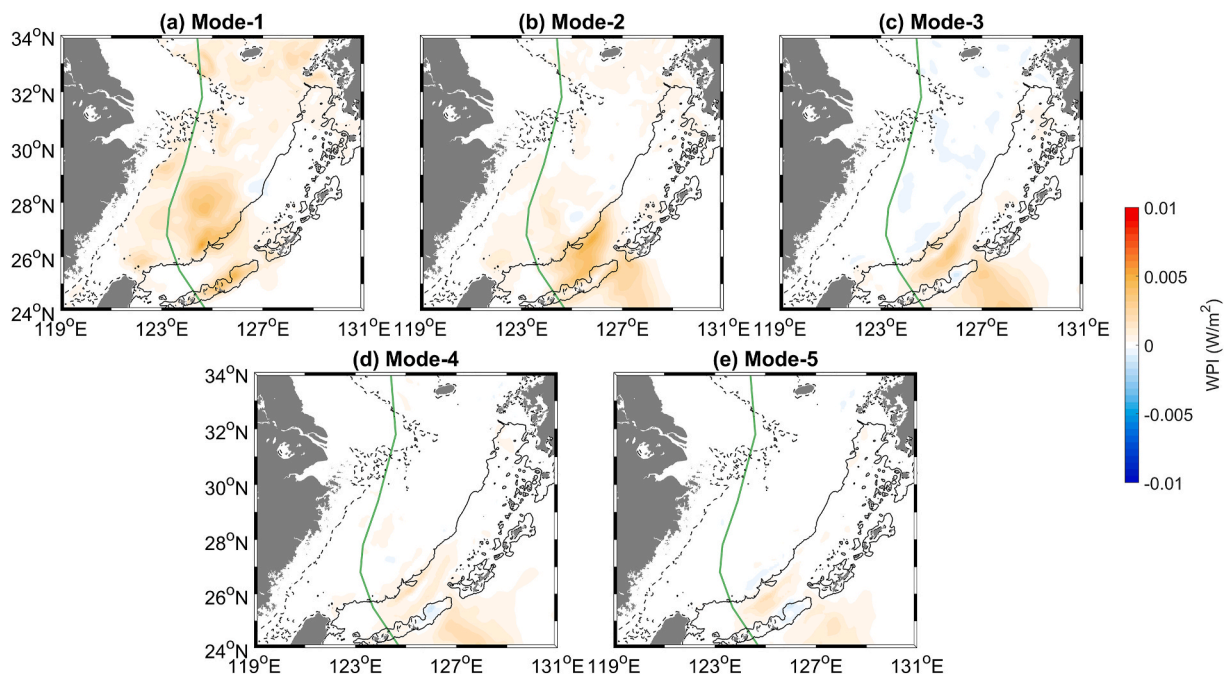


**Fig. 9.** Time-averaged modal WPI of (a–e) mode-1 to mode-5 for typhoon Meari. In each panel, the green curve denotes the typhoon track, and the black dashed and solid curves denote the 50 and 200 m isobaths, respectively.

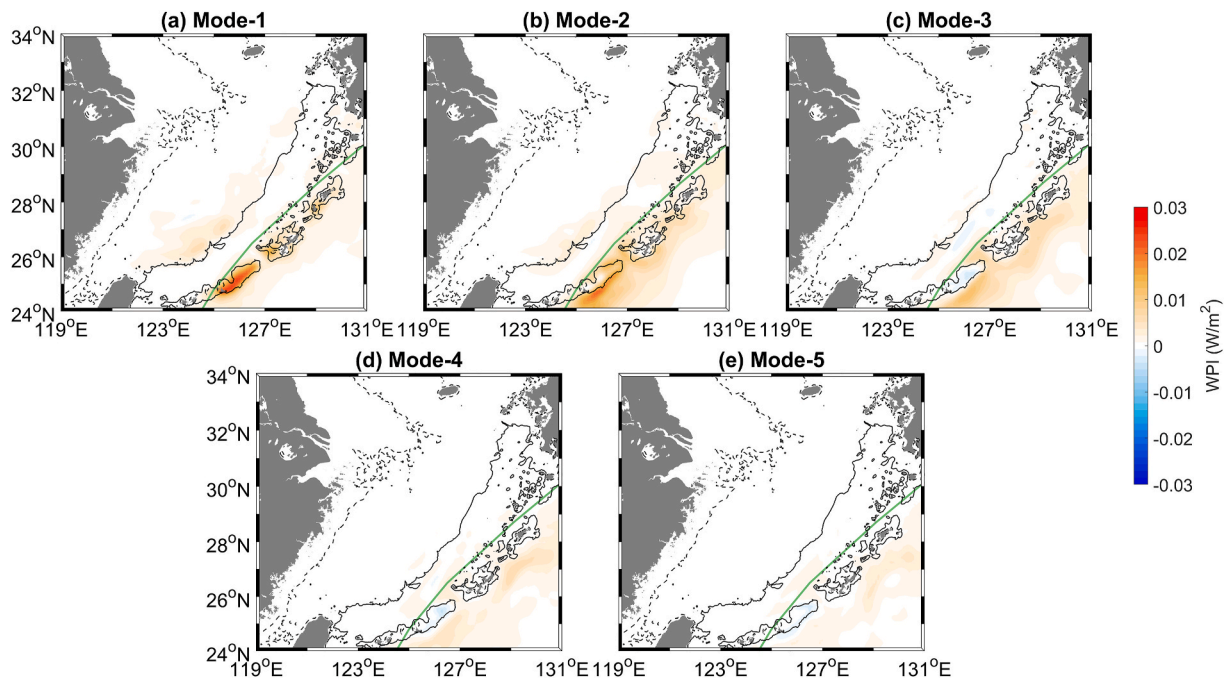


Fig. 10. Time-averaged modal WPI of (a–e) mode-1 to mode-5 for typhoon Songda. In each panel, the green curve denotes the typhoon track, and the black dashed and solid curves denote the 50 and 200 m isobaths, respectively.

Okinawa Trough and northwest Pacific Ocean). This result indicates that the modal NIKE is also mainly generated locally.

However, the modal WPI is not the real cause for the modal content of typhoon-induced NIWs. According to Equation (6), the modal WPI equals to the dot product of wind stress and modal near-inertial velocity at the surface, of which the former is the same for different modes and the latter is the modal decomposition result. In other words, the modal WPI represents the energy flux from winds to NIWs of the certain mode, but it cannot explain why the NIWs of such mode are excited by the winds.

The theoretical framework developed by Kundu and Thomson (1985) is used to explain the modal content of typhoon-induced NIWs. The governing equations for the linearized inviscid near-inertial motion are:

$$\frac{\partial u}{\partial t} - fv = -\frac{1}{\rho_0} \frac{\partial p}{\partial x} + F, \tag{12a}$$

$$\frac{\partial v}{\partial t} + fu = -\frac{1}{\rho_0} \frac{\partial p}{\partial y} + G, \tag{12b}$$

$$\frac{\partial p}{\partial z} + \rho g = 0, \tag{12c}$$

$$\frac{\partial u}{\partial x} + \frac{\partial v}{\partial y} + \frac{\partial w}{\partial z} = 0, \tag{12d}$$

$$\frac{\partial \rho}{\partial t} - \frac{\rho_0 N^2 w}{g} = 0, \tag{12e}$$

in which,

$$F = \frac{\tau_x}{h\rho_0} \text{ and } G = \frac{\tau_y}{h\rho_0}, \tag{13}$$

are the wind forcing functions acted as a body force in the mixed layer ( $h$  is the mixed layer depth). Expanding the variables into modes, the horizontal momentum Equation (12a–b) become

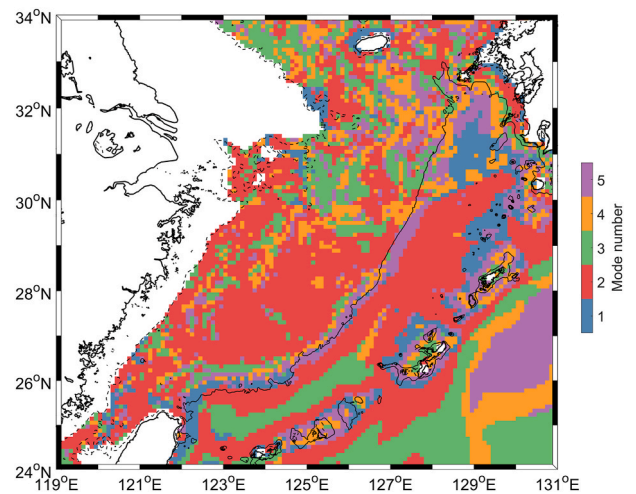


Fig. 11. Estimated dominant mode based on the theoretical framework of Kundu and Thomson (1985). The black dashed and solid curves denote the 50 and 200 m isobaths, respectively.

$$\frac{\partial u_m}{\partial t} - fv_m = -\frac{1}{\rho_0} \frac{\partial p_m}{\partial x} + F_m, \tag{14a}$$

$$\frac{\partial v_m}{\partial t} + fu_m = -\frac{1}{\rho_0} \frac{\partial p_m}{\partial y} + G_m, \tag{14b}$$

in which,

$$F_m = \frac{\tau_x}{\rho_0 \int_{-H}^0 \Pi_m^2 dz} \text{ and } G_m = \frac{\tau_y}{\rho_0 \int_{-H}^0 \Pi_m^2 dz}, \tag{15}$$

are the modal wind forcing. If we neglect the slight influence of air pressure, the modal wind forcing is the only cause for the modal NIWs. Therefore, we can approximately estimate the dominant mode of NIWs through comparing the wind forcing of different modes [according to

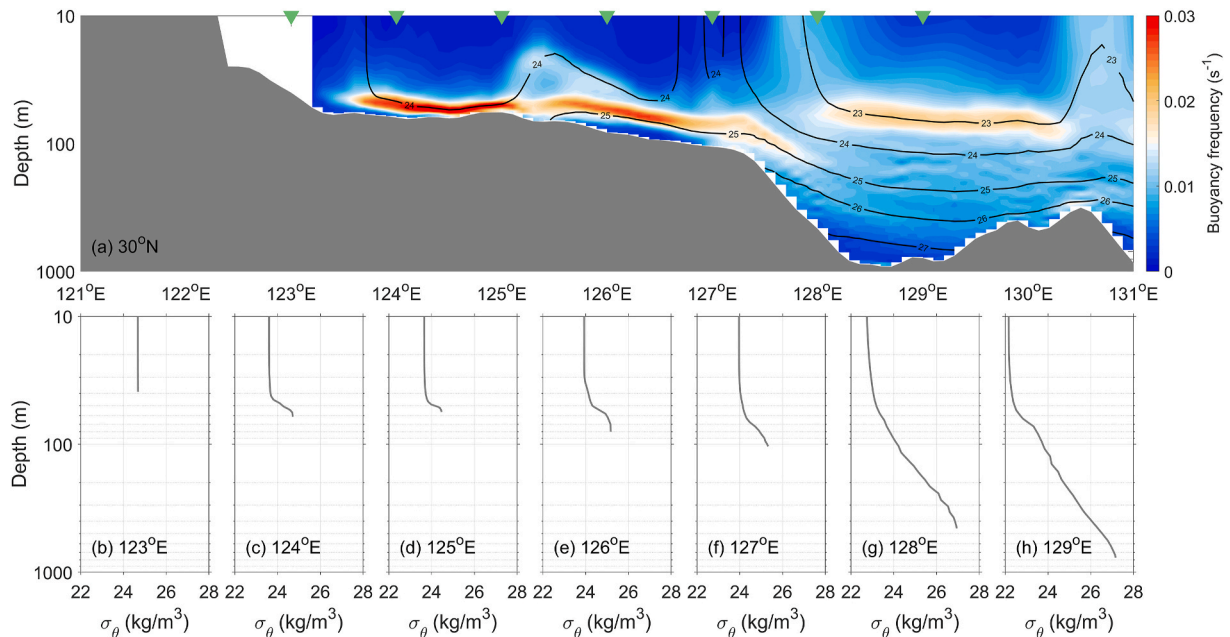


**Fig. 12.** (a) Buoyancy frequency (shading) and potential density anomaly ( $\sigma_\theta$ , contours, unit:  $\text{kg/m}^3$ ) along  $30^\circ\text{N}$  and vertical profiles of potential density anomaly at (b)  $123^\circ\text{E}$ , (c)  $124^\circ\text{E}$ , (d)  $125^\circ\text{E}$ , (e)  $126^\circ\text{E}$ , (f)  $127^\circ\text{E}$ , (g)  $128^\circ\text{E}$  and (h)  $129^\circ\text{E}$  along this section. The locations of these profiles are marked by green triangles in (a). Note that when the water depth is smaller than 50 m, the buoyancy frequency is not calculated and is not shown in (a). Also note that all the y-axes are in the log form.

Equation (15), the minimum value of  $\int_{-H}^0 \Pi_m^2 dz$  corresponds to the maximum modal wind forcing].

Take the result at  $128^\circ\text{E}$ ,  $24.8^\circ\text{N}$  as an example. According to the normal modes shown in Fig. 2b, the values of  $\int_{-H}^0 \Pi_m^2 dz$  for mode-1 to mode-5 are 413, 316, 289, 379 and 458, respectively. Because the value of  $\int_{-H}^0 \Pi_m^2 dz$  for mode-3 is the smallest among the five modes, the dominant mode of NIWs at  $128^\circ\text{E}$ ,  $24.8^\circ\text{N}$  is mode-3 according to the theoretical framework of Kundu and Thomson (1985). This result is consistent with the modal decomposition result (Fig. 5). Fig. 11 further shows the dominant mode of NIWs estimated from this theoretical framework. It is easy to find that in the deep regions of the domain, the estimated dominant mode is generally consistent with the modal decomposition results for typhoons Meari and Songda (Fig. 6f and 7f), i. e. mode-2 and mode-3 are dominant in the Okinawa Trough, and mode-3 to mode-5 are dominant in the northwest Pacific Ocean. The slight deviation between them can be explained, because the advection and dissipation are not considered in the theoretical framework (Equation (12)), but they do exist in the CROCO. Therefore, the dominance of higher-mode wind forcing is the cause for the dominance of higher-mode NIWs in the deep regions.

However, the result of the theoretical framework cannot account for the dominance of mode-1 NIWs in the shallow regions, as the wind forcing here is still dominated by higher modes (Fig. 11). Actually, the wind forcing is not the sole factor that determines the NIWs. The stratification also has a crucial influence on the NIWs. Fig. 12 shows the stratification along  $30^\circ\text{N}$  as an example. It is clearly shown that in the regions where water depth is smaller than 50 m, the density is nearly uniform in the vertical direction, indicating that no stratification is developed here (Fig. 12b). That's why we did not conduct modal decomposition in these regions (section 2). In the shallow regions where water depth is between 50 and 200 m, there exists two-layer-structure stratification (Fig. 12a, c–f), which can only support mode-1 internal waves in theory. In the deep regions where water depth is larger than 200 m, the two-layer-structure stratification disappears (Fig. 12a, g–h). Similar stratification can be found at other sections, which are not shown. Based on this result, we believe that the two-layer-structure

stratification is the cause for the dominance of mode-1 NIWs in the shallow regions. Note that such phenomenon (two-layer-structure stratification and dominance of mode-1 NIWs) also exists on the continental shelf of the Mid-Atlantic Bight (Zhang et al., 2018; Han and Yu, 2022).

Although this study only focuses on the modal content of NIWs induced by typhoons Songda and Meari around the ECS, the conclusions of this study can be extended to other oceans. Actually, NIWs dominated by mode-1 have been reported in many shallow regions, such as in the Yellow Sea (Yang et al., 2021), on the continental shelves of South China Sea (Yang et al., 2015) and Mid-Atlantic Bight (Zhang et al., 2018; Han and Yu, 2022), and NIWs dominated by higher modes have been found in the deep regions in the South China Sea (He et al., 2022) and global ocean (Raja et al., 2022).

## 5. Summary

In this study, the NIWs induced by typhoons Songda and Meari in the ECS and its adjacent deep waters are simulated based on the CROCO, and their characteristics, especially the modal content, are analyzed. Results indicate that the NIKE induced by the two typhoons shows different intensity and spatial distribution, but shares a common feature, i. e. the NIKE in the deep regions of the domain is apparently larger than that in the shallow regions, which is consistent with the WPI, suggesting that the NIKE is mainly generated locally. With respect to the modal content, it is found that in the shallow regions, the NIWs induced by the two typhoons are mainly dominated by mode-1, whereas in the deep regions, they are dominated by higher modes (mode-2 to mode-5). Through analysis, we find that two mechanisms account for this phenomenon. In the deep regions, the dominance of higher-mode wind forcing is the cause for the dominance of higher-mode NIWs. Whereas in the shallow regions, the two-layer-structure stratification is the cause for the dominance of mode-1 NIWs. Although this study only focuses on the NIWs induced by two typhoons around the ECS, the conclusions of this study can be extended to other oceans, as similar phenomenon has been reported in other oceans.

## Declaration of competing interest

The authors declare that they have no known competing financial interests or personal relationships that could have appeared to influence the work reported in this paper.

## Acknowledgements

The authors would like to deeply thank the two reviewers who provide constructive suggestions that greatly improve the manuscript.

This study is supported by the Zhejiang Provincial Natural Science Foundation of China (grant number: LY21D060005) and the China Scholarship Council (grant number: 202006325025). The authors also thank the support by Grants-in-Aid for Scientific Research (MEXT KAKENHI grant numbers: 19H05696/20H04319) and the JSPS Postdoctoral Fellowships for Research in Japan.

## References

- Alford, M.H., 2003. Improved global maps and 54-year history of wind-work on ocean inertial motions. *Geophys. Res. Lett.* 30 (8), 1424. <https://doi.org/10.1029/2002GL016614>.
- Alford, M.H., 2020. Revisiting near-inertial wind work: slab models, relative stress, and mixed layer deepening. *J. Phys. Oceanogr.* 50 (11), 3141–3156. <https://doi.org/10.1175/JPO-D-20-0105.1>.
- Alford, M.H., Cronin, M.F., Klymak, J.M., 2012. Annual cycle and depth penetration of wind-generated near-inertial internal waves at Ocean Station Papa in the northeast Pacific. *J. Phys. Oceanogr.* 42 (6), 889–909. <https://doi.org/10.1175/JPO-D-11-092.1>.
- Alford, M.H., MacKinnon, J.A., Simmons, H.L., Nash, J.D., 2016. Near-inertial internal gravity waves in the ocean. *Ann. Rev. Mar. Sci.* 8, 95–123. <https://doi.org/10.1146/annurev-marine-010814-015746>.
- Amante, C., Eakins, B.W., 2009. ETOPO1 1 Arc-Minute Global Relief Model: Procedures, Data Sources and Analysis. NOAA Technical Memorandum NESDIS NGDC-24. National Geophysical Data Center, NOAA. <https://doi.org/10.7289/V5C8276M>.
- Cao, A.-Z., Li, B.-T., Lv, X.-Q., 2015. Extraction of internal tidal currents and reconstruction of full-depth tidal currents from mooring observations. *J. Atmos. Ocean. Technol.* 32 (7), 1414–1424. <https://doi.org/10.1175/JTECH-D-14-00221.1>.
- Cao, A., Guo, Z., Lv, X., Song, J., Zhang, J., 2017. Coherent and incoherent features, seasonal behaviors and spatial variations of internal tides in the northern South China Sea. *J. Mar. Syst.* 172, 75–83. <https://doi.org/10.1016/j.jmarsys.2017.03.005>.
- Cao, A., Guo, Z., Song, J., Lv, X., He, H., Fan, W., 2018. Near-inertial waves and their underlying mechanisms based on the South China Sea internal wave experiment (2010–2011). *J. Geophys. Res.: Oceans* 123 (7), 5026–5040. <https://doi.org/10.1029/2018JC013753>.
- Chen, G., Xue, H., Wang, D., Xie, Q., 2013. Observed near-inertial kinetic energy in the northwestern South China Sea. *J. Geophys. Res.: Oceans* 118 (10), 4965–4977. <https://doi.org/10.1002/jgrc.20371>.
- Chen, S., Polton, J.A., Hu, J., Xing, J., 2015. Local inertial oscillations in the surface ocean generated by time-varying winds. *Ocean Dynam.* 65 (12), 1633–1641. <https://doi.org/10.1007/s10236-015-0899-6>.
- de Freitas, P.P., Amorim, F.D.L.L., Mill, G.N., da Costa, V.S., Gabioux, M., Cirano, M., Paiva, A.D.M., 2019. Observations of near-inertial oscillations along the Brazilian continental shelf break. *Ocean Dynam.* 69 (10), 1203–1215. <https://doi.org/10.1007/s10236-019-01296-w>.
- Egbert, G.D., Erofeeva, S.Y., 2002. Efficient inverse modeling of barotropic ocean tides. *J. Atmos. Ocean. Technol.* 19 (2), 183–204. [https://doi.org/10.1175/1520-0426\(2002\)019<0183:EIMOBO>2.0.CO;2](https://doi.org/10.1175/1520-0426(2002)019<0183:EIMOBO>2.0.CO;2).
- Furuichi, N., Hibiya, T., Niwa, Y., 2008. Model-predicted distribution of wind-induced internal wave energy in the world's oceans. *J. Geophys. Res.: Oceans* 113 (C9). <https://doi.org/10.1029/2008JC004768>.
- Guan, S., Zhao, W., Huthnance, J., Tian, J., Wang, J., 2014. Observed upper ocean response to typhoon Megi (2010) in the northern South China Sea. *J. Geophys. Res.: Oceans* 119, 3134–3157. <https://doi.org/10.1002/2013JC009661>.
- Han, P., Yu, X., 2022. A numerical study of near-inertial motions in the Mid-Atlantic Bight area induced by Hurricane Irene (2011). *Ocean Sci.* 18 (6), 1573–1590. <https://doi.org/10.5194/os-18-1573-2022>.
- He, H., Cao, A., Wang, Y., Song, J., 2022. Evolution of oceanic near-inertial waves induced by typhoon Sarika (2016) in the South China Sea. *Dynam. Atmos. Oceans* 100, 101332. <https://doi.org/10.1016/j.dynatmoce.2022.101332>.
- Jeon, C., Park, J.H., Nakamura, H., Nishina, A., Zhu, X.H., Kim, D.G., et al., 2019a. Poleward-propagating near-inertial waves enabled by the western boundary current. *Sci. Rep.* 9 (1), 1–7. <https://doi.org/10.1038/s41598-019-46364-9>.
- Jeon, C., Park, J.-H., Park, Y.-G., 2019b. Temporal and spatial variability of near-inertial waves in the East/Japan Sea from a high-resolution wind-forced ocean model. *J. Geophys. Res.: Oceans* 124, 6015–6029. <https://doi.org/10.1029/2018JC014802>.
- Jiang, J., Lu, Y., Perrie, W., 2005. Estimating the energy flux from the wind to ocean inertial motions: the sensitivity to surface wind fields. *Geophys. Res. Lett.* 32 (15). <https://doi.org/10.1029/2005GL023289>.
- Kawaguchi, Y., Wagawa, T., Igeta, Y., 2020. Near-inertial internal waves and multiple-inertial oscillations trapped by negative vorticity anomaly in the central Sea of Japan. *Prog. Oceanogr.* 181, 102240. <https://doi.org/10.1016/j.pcean.2019.102240>.
- Kundu, P.K., 1993. On internal waves generated by travelling wind. *J. Fluid Mech.* 254, 529–559. <https://doi.org/10.1017/S0022112093002241>.
- Kundu, P.K., Thomson, R.E., 1985. Inertial oscillations due to a moving front. *J. Phys. Oceanogr.* 15, 1076–1084. [https://doi.org/10.1175/1520-0485\(1985\)015<1076:IODTAM>2.0.CO;2](https://doi.org/10.1175/1520-0485(1985)015<1076:IODTAM>2.0.CO;2).
- Large, W.G., McWilliams, J.C., Doney, S.C., 1994. Oceanic vertical mixing: a review and a model with a nonlocal boundary layer parameterization. *Rev. Geophys.* 32, 363–403. <https://doi.org/10.1029/94RG01872>.
- Le Boyer, A., Alford, M.H., Pinkel, R., Hennon, T.D., Yang, Y.J., Ko, D., Nash, J., 2020. Frequency shift of near-inertial waves in the South China Sea. *J. Phys. Oceanogr.* 50 (5), 1121–1135. <https://doi.org/10.1175/JPO-D-19-0103.1>.
- Liu, Y., Jing, Z., Wu, L., 2019. Wind power on oceanic near-inertial oscillations in the Global Ocean estimated from surface drifters. *Geophys. Res. Lett.* 46 (5), 2647–2653. <https://doi.org/10.1029/2018GL081712>.
- MacKinnon, J.A., Zhao, Z., Whalen, C.B., Waterhouse, A.F., Trossman, D.S., Sun, O.M., et al., 2017. Climate process team on internal wave-driven ocean mixing. *Bull. Am. Meteorol. Soc.* 98 (11), 2429–2454. <https://doi.org/10.1175/BAMS-D-16-0030.1>.
- Munk, W., Wunsch, C., 1998. Abyssal recipes II: energetics of tidal and wind mixing. *Deep Sea Res. Oceanogr. Res. Pap.* 45 (12), 1977–2010. [https://doi.org/10.1016/S0967-0637\(98\)00070-3](https://doi.org/10.1016/S0967-0637(98)00070-3).
- Niwa, Y., Hibiya, T., 2011. Estimation of baroclinic tide energy available for deep ocean mixing based on three-dimensional global numerical simulations. *J. Oceanogr.* 67 (4), 493–502. <https://doi.org/10.1007/s10872-011-0052-1>.
- Oey, L.-Y., Ezer, T., Wang, D.-P., Fan, S.-J., Yin, X.-Q., 2006. Loop current warming by hurricane Wilma. *Geophys. Res. Lett.* 33, L08613. <https://doi.org/10.1029/2006GL025873>.
- Price, J.F., Sanford, T.B., Forristall, G.Z., 1994. Forced stage response to a moving hurricane. *J. Phys. Oceanogr.* 24 (2), 233–260. [https://doi.org/10.1175/1520-0485\(1994\)024<0233:FSRTAM>2.0.CO;2](https://doi.org/10.1175/1520-0485(1994)024<0233:FSRTAM>2.0.CO;2).
- Qiao, M., Cao, A., Song, J., Pan, Y., He, H., 2022. Enhanced turbulent mixing in the upper ocean induced by super typhoon goni (2015). *Rem. Sens.* 14 (10), 2300. <https://doi.org/10.3390/rs14102300>.
- Raja, K.J., Buijsman, M.C., Shriver, J.F., Arbic, B.K., Siyanbola, O., 2022. Near-inertial wave energetics modulated by background flows in a global model simulation. *J. Phys. Oceanogr.* 52 (5), 823–840. <https://doi.org/10.1175/JPO-D-21-0130.1>.
- Sanford, T.B., Ma, B.B., Alford, M.H., 2021. Stalling and dissipation of a near-inertial wave (NIW) in an anticyclonic ocean eddy: direct determination of group velocity and comparison with theory. *J. Geophys. Res.: Oceans* 126 (5), e2020JC016742. <https://doi.org/10.1029/2020JC016742>.
- Schlosser, T.L., Jones, N.L., Bluteau, C.E., Alford, M.H., Ivey, G.N., Lucas, A.J., 2019. Generation and propagation of near-inertial waves in a baroclinic current on the Tasmanian shelf. *J. Phys. Oceanogr.* 49 (10), 2653–2667. <https://doi.org/10.1175/JPO-D-18-0208.1>.
- Simmons, H.L., Hallberg, R.W., Arbic, B.K., 2004. Internal wave generation in a global baroclinic tide model. *Deep Sea Res. Part II Top. Stud. Oceanogr.* 51 (25–26), 3043–3068. <https://doi.org/10.1016/j.dsr2.2004.09.015>.
- Whalen, C.B., De Lavergne, C., Naveira Garabato, A.C., Klymak, J.M., Mackinnon, J.A., Sheen, K.L., 2020. Internal wave-driven mixing: geophysical processes and consequences for climate. *Nat. Rev. Earth Environ.* 1 (11), 606–621. <https://doi.org/10.1038/s43017-020-0097-z>.
- Yang, B., Hou, Y., Hu, P., Liu, Z., Liu, Y., 2015. Shallow ocean response to tropical cyclones observed on the continental shelf of the northwestern South China Sea. *J. Geophys. Res.: Oceans* 120 (5), 3817–3836. <https://doi.org/10.1002/2015JC010783>.
- Yang, W., Wei, H., Liu, Z., Li, G., 2021. Intermittent intense thermocline shear associated with wind-forced near-inertial internal waves in a summer stratified temperate shelf sea. *J. Geophys. Res.: Oceans* 126 (12), e2021JC017576. <https://doi.org/10.1029/2021JC017576>.
- Ying, M., Zhang, W., Yu, H., Lu, X., Feng, J., Fan, Y., et al., 2014. An overview of the China Meteorological Administration tropical cyclone database. *J. Atmos. Ocean. Technol.* 31 (2), 287–301. <https://doi.org/10.1175/JTECH-D-12-00119.1>.
- Yu, X., Naveira Garabato, A.C., Vic, C., Gula, J., Savage, A.C., Wang, J., et al., 2022. Observed equatorward propagation and chimney effect of near-inertial waves in the midlatitude ocean. *Geophys. Res. Lett.* 49 (13), e2022GL098522. <https://doi.org/10.1029/2022GL098522>.
- Zhang, F., Li, M., Miles, T., 2018. Generation of near-inertial currents on the mid-atlantic Bight by hurricane arthur (2014). *J. Geophys. Res.: Oceans* 123, 3100–3116. <https://doi.org/10.1029/2017JC013584>.
- Zhao, Z., Alford, M.H., MacKinnon, J.A., Pinkel, R., 2010. Long-range propagation of the semi-diurnal internal tide from the Hawaiian Ridge. *J. Phys. Oceanogr.* 40 (4), 713–736. <https://doi.org/10.1175/2009JPO4207.1>.